Intrinsic localized modes in two-dimensional vibrations of crystalline pillars and their application for sensing

Daniel Brake[1,*], Huiwen Xu[2], Andrew Hollowell[2], Ganesh Balakrishnan[2], Chris Hains[2], Mario Marconi[3], and Vakhtang Putkaradze[4]

[1] Department of Mathematics, Colorado State University

[2] Center for High Tech Materials, University of New Mexico Albuquerque NM

[3] Department of Electrical Engineering, Colorado State University, Fort Collins CO 80523

[4] Department of Mathematics, University of Alberta, CAB 632, Edmonton, AB T6G 2G1

*Corresponding author; email: brake@math.colostate.edu

We present a complete analysis on the possibility of exciting and observing the Intrinsic Localized Modes (ILMs) in a crystalline linear array of nano pillars. We discuss the the nano-fabrication techniques for these arrays and visualization procedures to observe the real-time dynamics. As a consequence, we extend previous models to the study of two dimensional vibrations to be consistent with these restrictions. For these pillars, the elastic properties and hence the dynamics depend on the pillar's shape and the orientation of the crystal axes. We show that ILMs do form in the system, but their stability, defect pinning and reaction to friction strongly depend on the crystals properties, with the optimal dynamics only achieved in a rather small region of the parameter space. We also demonstrate fabrication techniques for these pillars and discuss the applications of these pillar arrays to sensing.

I. INTRODUCTION

There has been substantial interest in application of micro- and nano-scale resonators to sensing. The majority of previous studies employing micromechanical cantilevers for use in sensing have monitored frequency shift upon attachment of particles or molecules [1–11]. It has been demonstrated that micro- and nano mechanical sensors can afford single molecule, or even atom, sensitivity. This is achieved by producing a very high Q-factor resonator and measuring frequency shift upon attachment of a particle. The use of multiple resonators has been suggested for multi-channel sensing applications [12]. However, as far as we are aware, there has not been any work on single molecule detection utilizing the *amplitude* of oscillations of nano mechanical arrays, although these ideas have been tested on the micro scale, see *e.g.* [13].

ILMs have appeared in a large variety of oscillatory systems where nearest neighbor coupling and nonlinearity are present. These coherent oscillations, where most of the energy focuses in a single oscillatory pillar, were first discovered over 20 years ago [14, 15]. In some literature, ILMs have also been referred to as discrete breathers, but for consistency in this paper we shall keep the name ILM. Since then, ILMs have then been found in a wide variety of structures and there has been substantial interest in the theoretical analysis and practical applications of ILMs [16–28]. In general, most of these works have concentrated on the analysis of the oscillations being described by one variable. In particular case of ILM in cantilever arrays, the one-dimensionality of vibrations was enforced by designing the experiments with the cantilever thickness in the direction of vibration to be much smaller than in the other direction.

In this paper, we outline the feasibility of using the amplitude of nonlinear oscillations of multi-pillar arrays with nanometer dimensions for sensing. In particular, we concentrate on the excitement and control of nonlinear oscillations known as Intrinsic Localized Modes, or ILMs. The ILM dynamics can be used to implement a high resolution sensor with the capability to perform single molecule detection. The detection concept is based on the study of the ILM configuration that is established in an array of nano-scale mechanical oscillators when a molecule attaches to one of the elements of the array. An attachment will introduce an anisotropy in the array that could be detected due to the change in the ILM configuration. To realize this idea three challenges have to be

overcome: a comprehensive numerical simulation that will allow to understand the ILM formation and temporal evolution, a precise fabrication protocol for the nanopillar array compatible with the constraints of the experiment, and a suitable detection system that will allow to visualize the nanopillar oscillations and study the ILM evolution. In the following sections we will provide a detailed description on how these three challenges can be effectively accomplished.

The scaling of ILM-based sensors to nanoscale presents several challenges, the most important being visualization of motion. Traditional scanning microscopy techniques that have the capability to resolve nanometer scale structures do not allow to perform time-resolved images. We show, however, that it is possible to create an array with observable ILMs and record the oscillatory dynamics of the array if one utilizes the technique of EUV flash holography. Holographic imaging can achieve a high spatial resolution in the plane perpendicular to the illumination axis, while it has a much poorer resolution in the longitudinal direction. This technique thus limits the observation to oscillations parallel to the pillar array, as opposed to the transversal oscillations that were considered before [22, 24, 29]. Thus, it is essential to consider arrays capable of exciting two dimensional vibrations, and treat only the parallel vibrations as observables.

The two-dimensional motion of the pillars is similar to having two coupled oscillator arrays, or an array of oscillators with an internal degree of freedom. We undertake a detailed analysis of ILM appearance in the realistic models of these vibrations. Friction has been ignored in most previous works on the subject, but we felt that it is essential to incorporate it for nanoscale dynamics as the system vibrating at MHz frequency will undergo millions of oscillations per visualization sapling time (fraction of Hz). Based on the estimates provided in the literature, we also introduce friction in the system and show that it plays an essential role in stabilizing ILM dynamics. The conclusion of this work is the excitement and direct visualization of ILM in realistic system of nano pillar arrays is possible, but the application to sensing strongly depend on the geometry and elastic properties of the fabricated array.

II. SETUP OF THE MODELING PROBLEM

We model bidirectional vibrations of an infinite array of crystalline pillars. For simplicity, in this paper we assume that each crystalline pillar: has square cross-section; that the flat sides are parallel to the axis of the array; the two axes are perpendicular to each other; and the crystalline substrate connecting the pillars functions as a coupling mechanism.

These cantilever arrays, when driven by an external vibration source, function as coupled oscillators. The material properties determining the governing differential equations are a two-direction generalization of the nonlinear equations for pillar vibrations derived in [22, 24]. In order to reliably pin the ILM to the desirable location (center pillar), we introduce a small defect in that pillar's properties, represented mathematically as a modification of the ODE parameter α_1, and make sure that the ILM is attractive to the defect's location in the array. The setup for the problem of interest is shown on Fig. 1. In an experiment with sub-micron nano pillar arrays, the forcing will most likely be distributed among many pillars, and artificial preparation of an ILM will be experimentally unfeasible. Thus, in our simulations, we have analyzed ILMs that spontaneously and robustly appear from random initial conditions, under the influence of distributed forcing.

The equations of motion for the pillars are formulated as follows. Suppose $u_{k,x}$ and $u_{k,y}$ are deflections of the pillar tips in the parallel (x) and transversal (y) directions to the array, as shown on Fig. 1. Note that these two components of the pillar deflection are not necessarily aligned with the crystal axes. We compute the linear components of the stress by supposing for the given deflection, the quadratic part of deformation energy of an individual pillar is given by the quadratic form $E_2 = \frac{1}{2}\mathbf{u}_k^T Q_2 \mathbf{u}_k$. For the purpose of this paper, we choose a parameterization of the symmetric matrix Q_2 with three parameters $\alpha_{1,x}$, $\alpha_{1,y}$ and α_3 as follows:

$$E_{2,I} = \frac{1}{2}\sum_k \alpha_{1,x} u_{k,x}^2 + \alpha_{1,y} u_{k,y}^2 + \alpha_3 \big(u_{k,x} - u_{k,y}\big)^2, \tag{1}$$

where the index I stands for the quadratic energy of an individual pillar. There is also

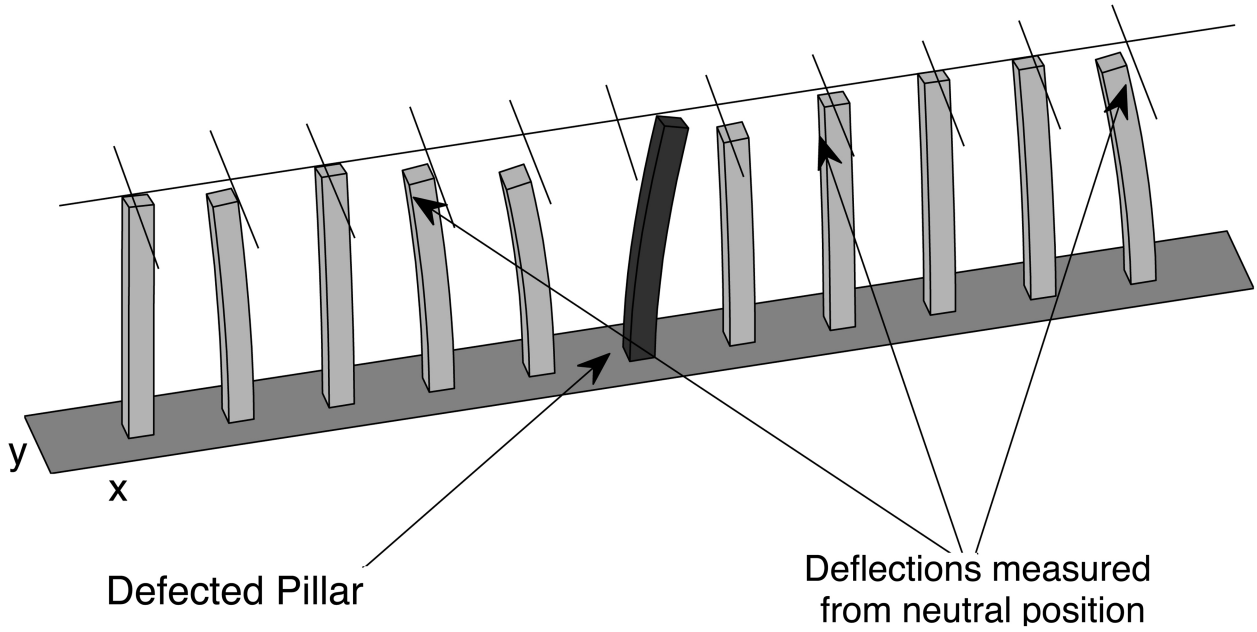

FIG. 1. An illustration of one dimensional cantilever array that is able to undergo vibrations in two directions. For explanation, we have also drawn a defected pillar that is used to pin the ILM appearing from random initial condition on the center pillar.

a quadratic coupling term which we shall take to be

$$E_{2,C} = \frac{1}{2}\sum_k \alpha_{2,x}\big(u_{k,x} - u_{k-1,x}\big)^2 + \alpha_{2,y}\big(u_{k,y} - u_{k-1,y}\big)^2 . \tag{2}$$

Then for a rectangular pillar made out of uniform material with Young's modulus E and density ρ, with the dimensions w_x (width), w_y (thickness) and l (height), the frequencies of *linear* vibrations in the x and y directions are

$$\nu_x \simeq 0.56\sqrt{\frac{E}{\rho}\frac{I_x}{Al^4}}\,, \quad \nu_y \simeq 0.56\sqrt{\frac{E}{\rho}\frac{I_y}{Al^4}}\,, \tag{3}$$

where $A = w_x w_y$ is the cross-sectional area of the pillar, and $I_x = w_x w_y^3/12$ and $I_y = w_y w_x^3/12$ are the bending momenta in the x and y directions respectively. For the crystal structure, there is also difference in Young's modulus in different directions. A typical value of vibrational frequency of a GaAs pillar with $w_x = w_y = 200$ nm and $l = 5\mu$m is about 3.2 MHz.

One of the parameters of $\alpha_{1,x}$ or $\alpha_{1,y}$ can be normalized to 1 by properly rescaling time, so in the new time $\tau = 1$ corresponds to one period of vibration. In what follows, we shall make additional simplification and consider $\alpha_{1,x} = \alpha_{1,y} = 1$, which happens *e.g.* for the case of material with cubic lattice aligned with the coordinate axes x and y, and thicknesses of the material in x and y directions adjusted properly. It is not essential simplification as far as physics is concerned, but it allows us to cut down on the number of parameters analyzed.

The parameters $\alpha_{2,x}$ and $\alpha_{2,y}$ can be derived analytically in terms of material properties of the pillars and geometric dimensions of the array [30]. This derivation is quite cumbersome and we shall not present it here. We shall just assume, for simplicity, $\alpha_{2,x} = \alpha_{2,y} = \alpha_2$ which we treat as a parameter. Physically, such situation can be realized by adjusting the thickness of each pillar and the distance between the pillars. it is not an essential for further considerations, but it does cut down the number of parameters to study.The normalization used in this paper gives the typical values of α_2 to be around 0.1 for realistic materials and dimensions used, but it can also be as small as 0.02 and as large as 0.5. Then, we study the behavior of the system as a function of parameters α_2 and α_3. Also, it is important to notice that the eigenvalues of the Hessian of this matrix are strictly positive for $\alpha_2 > 0$ and $\alpha_3 > 0$ so there are no degeneracies or unphysical values of parameters in the system.

The nonlinear (cubic) term in the equation leads to the fourth order term in energy, described by a fourth order tensor Q_4, *i.e.*, $E_4 = Q_4 \cdot \mathbf{u}_k \cdot \mathbf{u}_k \cdot \mathbf{u}_k \cdot \mathbf{u}_k$. Even when proper symmetries are included, the number of non-zero components of Q_4 lead to the exceedingly large number of parameters. It is possible to estimate some of these components analytically if the information about the orientation of crystalline axes, pillar shape and nonlinear elasticity is known. This will be done in further studies; for the purpose of this work, we shall consider a simpler particular case of the nonlinear individual energy as

$$E_{4,I} = \frac{1}{4}\sum_k \beta_1\Big(u_{k,x}^4 + u_{k,y}^4\Big) + \beta_3\Big(u_{k,x} - u_{k,y}\Big)^4, \tag{4}$$

and the nonlinear coupling energy as

$$E_{4,C} = \frac{1}{4}\sum_k \beta_2\Big((u_{k,x} - u_{k-1,x})^4 + (u_{k,y} - u_{k-1,y})^4\Big). \tag{5}$$

We shall note that theoretical expressions for the parameters α_i and β_i have been derived previously as a function of material parameters and geometric dimensions of the pillars [22, 24–26]. The coefficients for the individual beam can be derived from the nonlinear Euler-Bernoulli beam theory. If u is measured as a fraction of cross-section w_x, for example, then $\beta_1/\alpha_1 \sim C_1 w_x^2/L^2$, with the non-dimensionalized prefactor C_1 depending on the normalization of w_x chosen, typically being of order 1. Depending on the geometry, the nonlinear coupling theory gives $\beta_{2,3}/\beta_1 \sim 0.1 \div 1$. However, we must note that the nonlinear coupling terms β_2 and β_3, while have been derived analytically, in general do not fit experimentally observed parameters [30]. Thus, we shall treat the values of β_2 and β_3 as variables that are approximately of the same order. In what follows, we shall also keep the typical parameter scaling found previous works $\alpha_2/\alpha_1 \sim \beta_2/\beta_1 \sim 0.1$, although we do allow it to vary along the scan of the parameter domain.

The total potential energy is then $E = E_{2,I}+E_{2,C}+E_{4,I}+E_{4,C}$. For symmetry reasons, in the case considered here there is no cubic term in the energy. However, note that a cubic term may appear for a general arrangement of the crystal axes and pillar facets, in the geometries breaking the reflection symmetry of the system. The appearance and role of a cubic term in energy, leading to quadratic terms in the equations, is very interesting and will be addressed in further studies. However, this will lead to the necessity of investigation of a large number of parameters, which will be the object of further study. The corresponding equations of motion for two directions are

$$\begin{aligned}
\ddot{u}_{k,x} = &- \alpha_{1,x} u_{k,x} - \alpha_2\big((u_{k,x} - u_{k-1,x}) + (u_{k,x} - u_{k+1,x})\big) \\
&- \beta_1 u_{k,x}^3 - \beta_2\big((u_{k,x} - u_{k-1,x})^3 + (u_{k,x} - u_{k+1,x})^3\big) \\
&- \alpha_3(u_{k,x} - u_{k,y}) - \beta_3(u_{k,x} - u_{k,y})^3 \\
&- \gamma \dot{u}_{k,x} + \sigma \sin(t)\,, \qquad (6) \\
\ddot{u}_{k,y} = &- \alpha_{1,y} u_{k,y} - \alpha_2\big((u_{k,y} - u_{k-1,y}) + (u_{k,y} - u_{k+1,y})\big) \\
&- \beta_1 u_{k,y}^3 - \beta_2\big((u_{k,y} - u_{k-1,y})^3 + (u_{k,y} - u_{k+1,y})^3\big) \\
&- \alpha_3(u_{k,y} - u_{k,x}) - \beta_3(u_{k,y} - u_{k,x})^3 \\
&- \gamma \dot{u}_{k,y} + \sigma \sin(t)\,. \qquad (7)
\end{aligned}$$

This functional form of directional coupling allows a comprehensive study of ILM formation for two parameters, α_2, α_3 and β_3. In addition, we have added the dissipation

Physical Meaning	Parameter	Values
Individual frequency of one pillar	α_1	1
Linear coupling, same direction	α_2	$0.02 \ldots 0.5$
Linear coupling, different directions	α_3	$0.02 \ldots 0.5$
Nonlinearity in one pillar	β_1	0.01
Nonlinear coupling, same direction	β_2	$0.0002 \ldots 0.01$
Nonlinear coupling, different directions	β_3	$0.0002 \ldots 0.01$
Dissipation	$\gamma = 1/Q$	0.0001
Forcing	σ	0.001

TABLE I. Values of parameters used in simulations

in the pillars, described by the term $\gamma \dot{\mathbf{u}}_k$, and the forcing term, proportional to σ. The coupling parameters α_3 and β_3 can be estimated numerically, but their precise value for a given experiment is generally unknown. Thus, they must be treated as parameters in the problem.

III. SIMULATION RESULTS

Here, we present the results for spontaneous formation of ILMs in the system. The values of the parameters used are presented in the table below. While the typical value of α_1 are around 1, we have chosen to scan a large set of values in order to accommodate both cases when there is large discrepancy in natural frequencies in two directions, and, alternatively, when the natural frequencies of vibration are very close to each other. Note that in our normalization, the Q-factor for an individual oscillator is simply $Q = 1/\gamma$, although there are some discrepancies in the pre factor of that expression because of different definitions. Experimentally measured values of Q factors for micro cantilevers are in the range of 10^4, but it could be smaller for small nano-resonators considered here, as the internal dissipation in nano materials is not well understood. While this is commonly considered to be a very high Q, we believe it is important to introduce friction in the simulations, since we are interested in the very long time scales. As it turns out, small friction makes it much easier for ILMs to appear and pin on the defect,

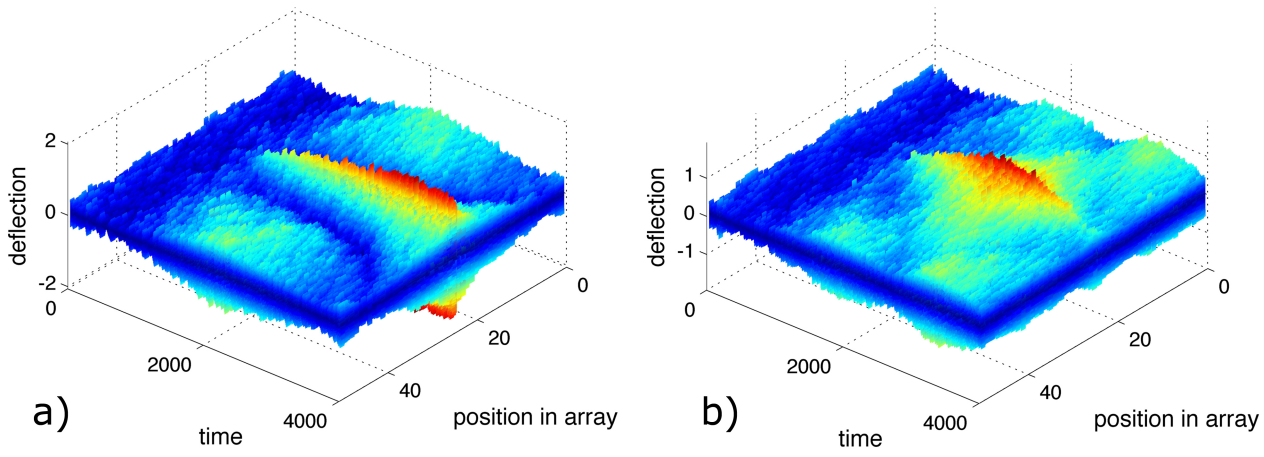

FIG. 2. Left: ILM spontaneously forming under dissipative driven conditions, with detectability ~ 3.8. Right: Failure of ILM to form, detectability ~ 1. The vertical axis denotes amplitude of deflection; time and pillar number make the two horizontal axes.

taken over very long times that are of interest for the application described in this work.

A short discussion of the forcing term is warranted here as well. It is possible to obtain piezoelectric driver for the pillar at the frequencies we consider here (several MHz), but it is hard to estimate the amplitude of such driver as delivered to pillars. Instead, we take an alternative approach and use the idea of electrostatic driving of pillars that have been charged by ion bombardment [31]. Using estimates for a typical density of ions in the pillars from [31], we conclude that if the deflection is measured as a fraction of w_x, then the necessary electric field for the *static* deflection σ is given by $E = \sigma(w_x/L)^4 \cdot 4.65 \cdot 10^{11}$ V/m. For example, for the aspect ratio $w_x/L = 0.1$ and $\sigma = 10^{-4}$, the necessary electric field will be 4650 V/m, which is easily realizable in experiment.

In order to relate our simulations to sensor applications, which would detect defects caused by molecule attachment to a pillar along an array, we put a 1% defect in α_1 for the pillar in the middle of the array. When the dissipation is present, ILM defect pinning seems to be enhanced. This is in contrast with previous results on defect detection in systems without dissipation [24, 25] where pinning on the defect was shown to be of rather sensitive nature. In any case, the formation of ILM in the nano pillar array is

quite common – our calculations show that ILM tend to robustly appear for a large value of parameters; a typical example of ILM formation is shown on Figure 2.

Nanoscale sensor applications of ILMs would exploit detection of oscillation amplitude for each pillar, as discussed in Section V, on a linear comb-like crystalline array. An individual pillar would be on the order of 100nm, with resonant frequencies in the hundreds of MHz. Hence, it is important to see how practical it is to detect a defect using ILMs. This is different from simply observing ILM formation. We define the ILM detectability as the energy concentrated in an ILM divided by the average energy of all other pillars (this energy is non-zero due to the competition between the forcing and dissipation). This observable measures how likely we are to detect a defect by ILM pinning; detectability values higher than unity correspond to more likely detection, while detectability ~ 1 indicates uniform distribution of energy.

Our results are presented on Fig. 3. Each point on this plot is the result of ten simulations until $t = 1000$, with the amplitude of ILM computed from the last third of the time interval. The horizontal and vertical axes are: on the left, α_2 and α_3, and on the right β_2 and β_3. Red areas represent high values of detectability, and blue represent the low values. As we see, there are areas of parameter where ILM appearance is very robust; however, these areas are relatively small. There is a highly intricate pattern describing high detectability of ILMs, and it is more typical to observe the energy concentration in ILM to be rather small for small defect percentages, as is evident from our results. Larger parameter defects induce stronger pinning. Thus, the work presented here warrants more detailed studies of ILM formation and detectability, and the necessity of improved design of nano pillar arrays for nanotechnology applications.

IV. NANOFABRICATION

The fabrication of the nano pillar arrays required for an ILM demonstration at the nanometer scale requires the single crystal ensembles fabricated to a very high level of precision. The techniques that can be used for such fabrication can be classified as - epitaxially grown nano pillars, etched nano pillars and ion beam written nano pillars. The epitaxial techniques are capable of producing large scale arrays of pillar arrays of correct scale [32]. However, in spite of our best efforts, we could not reliably produce

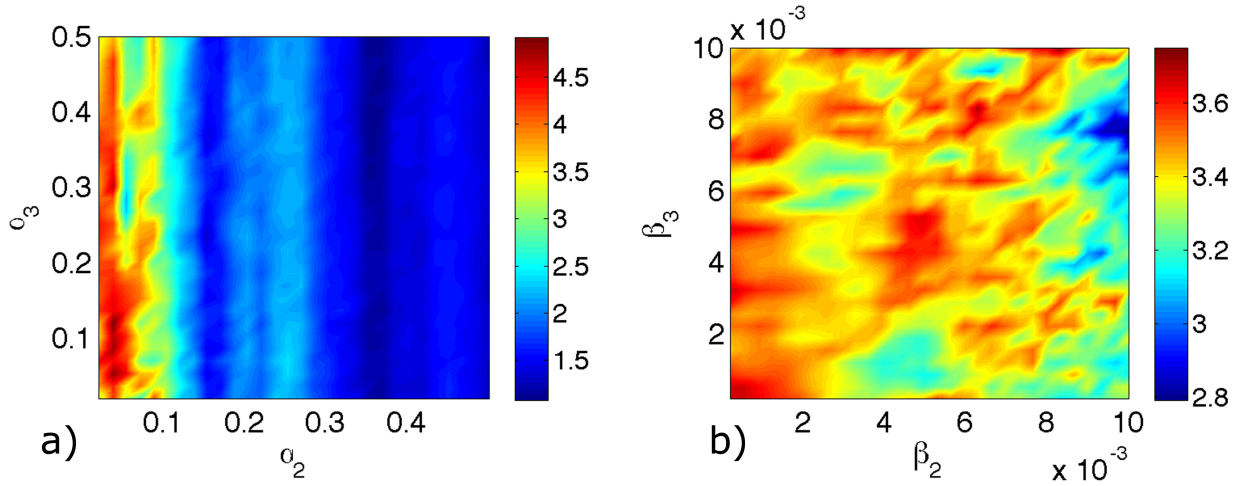

FIG. 3. Phase diagram for ILM detectability at defected pillar in 50-pillar crystal array. Coupling parameters α_2 and α_3 are examined in the left, β_2 and β_3 in the right. Red areas denotes strong ILM formation whereas blue indicates practically no spontaneously forming ILMs present in the system.

linear arrays of nano pillars using either selective area epitaxy [33] or vapor-liquid-solid (VLS) [34] method for pillar growth; the variation from pillar to pillar was excessive. The use of an etch-down process [35] was also difficult since in this case we would have to define mesas in the nanometer scale and etch down to several microns to define the pillar. However, we were successful in fabrication of the etched pillars by defining the pillars parallel to the plane of the substrate using a combination of lithography and dry/wet etches. The same form factor was also realized using ion beam based writers where instead of lithography the pillars were defined using ion or electron beam based ablation/writing. The ion beam based technique can produce arrays with lower number of pillars, but can achieve high accuracy and smaller cross-section. The remainder of this section is devoted to the description of these two techniques.

A. Dry etch

The fabrication of lithography based pillars is done on an epitaxially grown sample on a GaAs substrate. A 350nm thick layer of $Al_{0.95}Ga_{0.05}As$ is epitaxially grown on a

GaAs substrate using MBE with a subsequently grown layer of GaAs which serve as the material for pillar array. The thickness of this layer determines the transverse direction of the pillars. The $Al_{0.95}Ga_{0.05}As$ serves as an etch stop layer between the GaAs substrate and the epilayer of GaAs. Lithography techniques are used to pattern the topside of the wafer defining the dimensions of the arrays of cantilevers. A dry etch is used to etch the unmasked areas of the GaAs layer defining the pillars. The substrate is then backside patterned with a titanium (Ti) and nickel (Ni) metal stack and a selective wet etch is used to etch a window through the substrate stopping at the $Al_{0.95}Ga_{0.05}As$ etch stop layer. Once the $Al_{0.95}Ga_{0.05}A$ etch stop layer is removed with a hydro fluoric acid (HF) based buffer oxide etch (BOE) the cantilevers are effectively released from the substrate. Fig. 5 shows a 3D cross section of the array of GaAs cantilevers. Topside lithographic patterning of the wafer is done to define the GaAs cantilever arrays. To create a photoresist (PR) mold for the etching the pillars, we spin coat the wafer with 5 mls of AZ4330 PR at a speed of 2000 rpm for a total of 30 seconds. Following the spin, the wafer undergoes a pre-exposure, soft bake at 90°C for 3 minutes and is then allowed to cool to room temperature. An aligner with a chrome mask is then used to transfer the pillar array pattern into the PR with an exposure to 365nm light. Vacuum contact between the chrome mask and the substrate is required to ensure a vertical side wall profile in the PR, which is necessary for a controlled etch of the GaAs during the dry etch procedure. The exposed PR is then developed leaving the edge pattern for the pillars. After the topside lithography process is complete the substrate is subjected to a dry etch in order to etch the topside GaAs epilayer and define the dimensions of the cantilevers. The parameters of the dry etch flow rate, pressure, and temperature are 35 sccm BCl_3, 2.5mTorr, 25°C respectively.

Once the reactive ion etch of the top GaAs epilayer is complete, the backside of the substrate is patterned and etched using a selective wet etch thus releasing the pillars. Because of this variation in the etch rate it is impossible to precisely stop the etch process at the AlGaAs etch stop layer by simply timing each etch run. In order to control the etch process and stop of the appropriate depth we use of an interferometric etch monitor. The interferometer measures reflected signal from the sample, reaching the etch stop layer of AlGaAs is manifested by a sharp drop in amplitude of the reflected

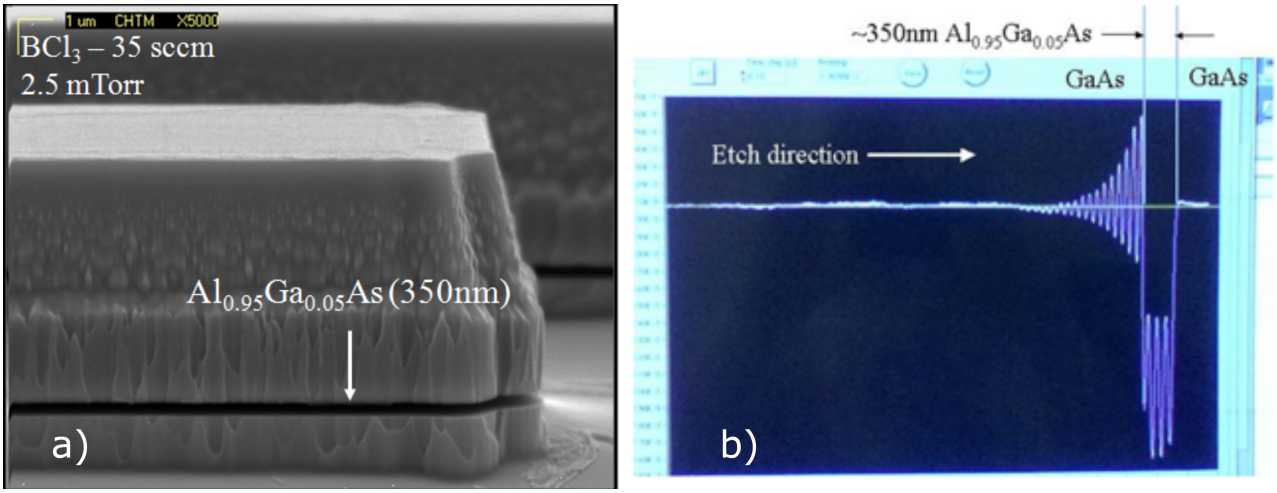

FIG. 4. Left: a sidewall profile of the etched GaAs cantilevers. Right: the interferometric etch monitor showing the change in oscillations with etch depth as well as change in refractive index between the GaAs and AlGaAs layers.

signal, as the Figure 4 demonstrates.

While the etching technique is rather effective and does produce large and consistent arrays, it has a drawback as pillars demonstrate certain variability arising from the backside window etch, as shown on Figure 4, left. Unfortunately, we were not able to consistently control the angle and shape of the pillars backside, which lead to variations of mass on the backside from pillar to pillar. This variation can be estimated as follows: if α is the typical angle of the etch on the backside, w_x is the thickness of the pillar and L its transversal length, then the typical uncertainty in pillars mass is $\Delta m/m \simeq w_x \tan\alpha/(2L)$. For $w_x \sim 1\mu$m, $\alpha \sim \pi/4$ and $L \sim 10\mu$m, the uncertainty in mass of a pillar due to the variation of the backside shape is estimated to be about 5%. Thus, while the process is highly suitable for creating large nano pillar arrays, if high consistency in pillars' mass is required, it may not be appropriate.

B. Ion Beam fabrication techniques

In order to circumvent the difficulties associated with etch techniques, we have therefore employed another method of pillar fabrication that is not limited by the lithography mask. We have made use of a FEI Quanta 3D Field Emission Gun SEM /Focused Ion

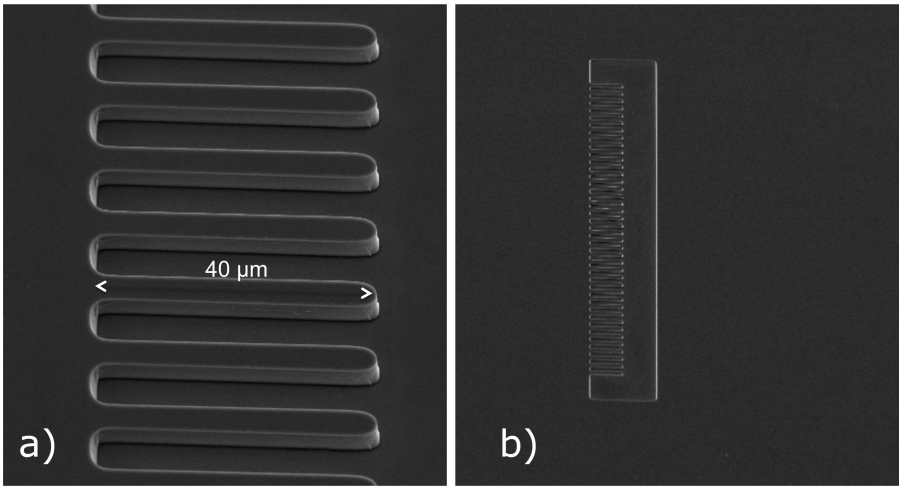

FIG. 5. An array of etched GaAs pillars with the pillars defined by a lithographic process followed by a RIE inductively coupled plasma etc.

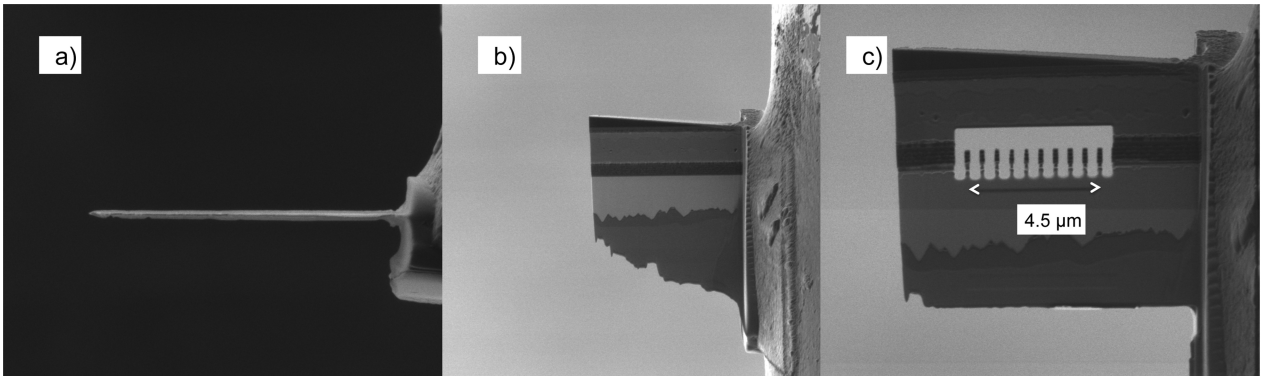

FIG. 6. Part a) of the figure shows a FIB thinned membrane of GaAs attached to a TEM grid. Part b) shows the plan view of the same membrane. Part c) shows the membrane with the nano pillar array written into it.

Beam (FIB) instrument. Using an beam of gallium ions we are, with a high precision, able to achieve nano pillar array prototypes with a wide range of dimensions and using several different materials. We are also able to define pillars using the FIB with the thickness of individual pillars of 100nm or less, in contrast the etching technique we describe in the previous section produces pillars with cross-sections of at least 500nm.

The process of creating the array using the FIB is as follows. A small section of the semiconductor is cut from substrate and attached to a transmission electron microscopy

grid. Once attached to the grid, the sample is thinned down using the focused ion beam to give it the correct thickness. This is shown in the part (a) (left, side view) and (b) (middle, plane view) of Fig. 6. The focused ion beam is now directed perpendicular to the sample and the window is now written into it. The finished array of pillars is shown in Fig. 6(c) (right). Thus using this method we can create nano pillar arrays with any crytallographic orientation and any dimension within the limit of the writing tool.

The Ion Beam technique demonstrates the ability to make prototype arrays suitable for dynamic investigations, albeit it is limited in scope to the production of 10-50 pillars because of the low speed, at least if realistic production time is assumed. However, the accuracy of this method is currently far superior to that of the dry etch method. In future works we shall consider whether it will be possible to enhance the accuracy of the dry etch method to approach that of the FIB technique.

V. VISUALIZATION USING EUV HOLOGRAM

We shall briefly describe the approach we followed to visualize the ILM dynamics using time-resolved flash extreme ultraviolet (EUV) holography. Techniques capable to form images without the use of lenses or mirrors have been widely used and found a vast range of applications in the optical regime. Lensless techniques are particularly advantageous in the EUV and X-ray region of the spectrum where complex optical elements are not available or difficult to implement. Besides its intrinsic experimental complexity, EUV imaging is particularly attractive due to the high spatial resolution that the short wavelength allows. Fourier transform holography [36–38] and iterative phase retrieval [39–41] are two different techniques which are employed in lensless EUV imaging.

We implemented a Fourier transform holographic set up with the illumination from a table top EUV capillary discharge laser. The holographic set up was realized with a Fresnel zone plate that is used as a beam splitter to generate the illumination and the reference beams, in a configuration similar to the one used by McNulty et al.[42]. In this configuration the laser beam is split by the zone plate into two beams: the zero order is used primarily as the illumination beam while the first order focus constitutes a spherical divergent wave that is used as the reference wave-front. A unique compact

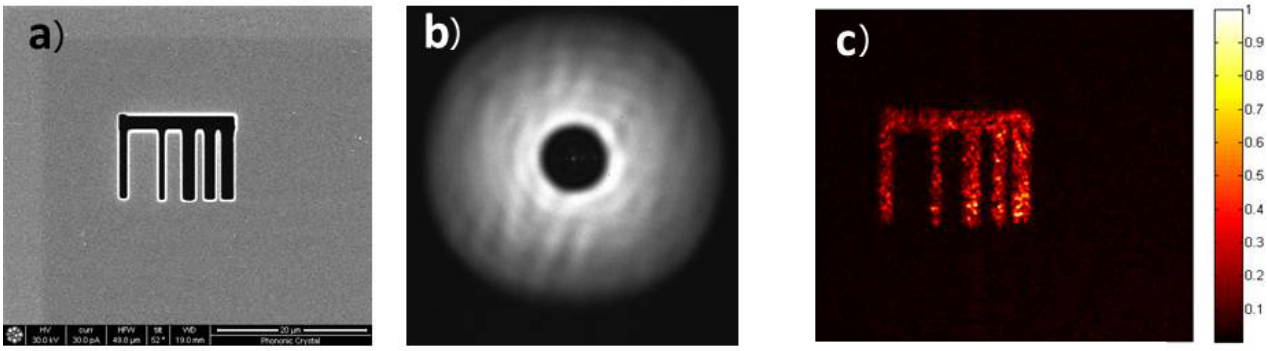

FIG. 7. a) SEM micrograph of the object used to test the Fourier holography setup, defined by focused ion milling in a 100 nm thick Si_3N_4 membrane. Four pillars shown on the picture have a width of 4.0, 2.44, 1.07 and 0.54 microns respectively. b) Singe shot hologram of the object shown in a). c) Reconstruction of the hologram. The four pillars are distinguishable in the image.

EUV laser capable to produce fully coherent spatial illumination at $\lambda = 46.9$ nm, with a pulse energy typically in the range of 0.5 mJ and a pulse-width of 1 ns FWHM was the illumination source[43, 44]. The hologram was recorded in a back illuminated CCD detector with 1 square inch area and 4 megapixels, and numerically reconstructed by direct two dimensional FFT. The object in this test was a series of pillars, with widths 4000, 2240, 1070 and 540 nm defined in a 15.4×11.4 μm^2 window fabricated in a 200 nm thick Si_3N_4 membrane. The object was fabricated using the focused ion milling tool described in a Section IV B. After the ion milling step a 200 nm thick layer of gold was deposited to increase the opacity of the sample. Figure 7(a) shows a SEM image of the object.

Single shot holograms, that yields a temporal resolution of 1 ns can be obtained with good S/N ratio. Figure 7(b) is a typical single shot hologram recorded under these conditions. A direct FFT transformation renders the image shown in Figure 7(c), where all the pillars are clearly visible. The resolution of the image is determined by the size of the reference beam, in this case 244 nm. However, it is important to notice that if necessary, the spatial resolution can be improved by replacing the Fresnel zone plate by another with higher numerical aperture that will generate a smaller focal point and

consequently improve the spatial resolution of the image or applying proper filtering and de-noising techniques.

The results shown in this section demonstrates the capability of the EUV holographic set up of obtaining time resolved images of extended objects (several microns) with a sufficient resolution to record the sub-micron pillars.

VI. CONCLUSION

In this paper, we have demonstrated feasibility of ILM formation for nano pillar arrays. We have shown that nano pillars of desired sizes can be fabricated and subsequently visualized using EUV single-shot holography method. Furthermore, ILM consistently appear in realistic models of vibrations of nano pillar array for a large variety of parameters, but the shape of ILM and sensitivity to the defect detection depends greatly on the size of the pillars and orientation of crystalline axes in the material.

ACKNOWLEDGEMENTS

We have benefitted from fruitful discussions with Profs. T. Hikihara, M. Kimura and M. Sato. This project received support from the Defense Threat Reduction Agency – Joint Science and Technology Office for Chemical and Biological Defense (Grant no. HDTRA1-10-1-007).

REFERENCES

[1] T. Thundat, G. Y. Chen, R. J. Wannack, D. P. Allison, and E. A. Wachter, Anal. Chem **67**, 519 (1995).

[2] C. Hierold, J. Micromech. Engr. **14**, S1 (2004).

[3] R. Mukhopadhyay, V. V. Sumbayev, M. Lorentzen, J. Kjems, P. A. Andreasen, and F. Besenbacher, Nano Lett. **5**, 2385 (2005).

[4] K. L. Ekinci and M. L. Roukes, Rev. Sci. Instruments **76**, 061101 (2005).

[5] L. Fischer, V. A. Wright, C. Guthy, N. Yang, M. T. McDermott, J. Buriakb, and S. Evoy, Sensors and Actuators B: Chemical **134**, 613617 (2008).

[6] L. Carrascosa, M. Moreno, M. Alvarez, and L. Lechuga, Trends in Anal. Chem. **25**, 196 (2006).

[7] J. Verd, A. Uranga, G. Abadal, J. Teva, F. Torres, F. Perez-Murano, J. Fraxedas, J. Esteve, and N. Barniol, Applied Physics Letters **91**, 013501 (2007).

[8] X. L. Feng, R. He, P. Yang, and M. L. Roukes, Nano Lett. **7**, 1953 (2007).

[9] M. Belov, N. J. Quitoriano, S. Sharma, W. K. Hiebert, T. I. Kamins, and S. Evoy, J. Applied Physics **103**, 074304 (2008).

[10] K. Jensen, K. Kim, and A. Zettl, Nature Nanotech. **3**, 533 (2008).

[11] E. Gil-Santos, D. Ramos, J. Martinez, M. Fernandez-Regulez, R. Garca, A. S. Paulo, M. Calleja, and J. Tamayo, Nano Lett. **5**, 641 (2010).

[12] J. Pepper, R. Noring, M. Klempner, B. Cunninghama, A. Petrovich, R. Bousquet, C. Clapp, J. Brady, and B. Hugha, Sensors and Actuators B: Chemical **96**, 565 (2003).

[13] M. Sato and A. J. Sievers, Low Temperature Physics **34**, 543 (2008).

[14] A. J. Sievers and S. Takeno, Phys. Rev. Lett. **61**, 970 (1988).

[15] J. B. Page, Phys. Rev. B **41**, 7835 (1990).

[16] P. G. Kevrekidis, A. R. Bishop, and K. O. Rasmussen, Phys. Rev. E **63**, 036603 (2001).

[17] P. G. Kevrekidis and V. V. Konotop, Phys. Rev. E **65**, 066614 (2002).

[18] M. Sato, B. E. Hubbard, L. Q. English, A. J. Sievers, B. Ilic, D. A. Czaplewski, and H. G. Craighead, Chaos **13**, 702 (2003).

[19] M. Sato, B. E. Hubbard, A. J. Sievers, B. Ilic, D. A. Czaplewski, and H. G. Craighead, Phys. Rev. Lett. **90**, 044102 (2003).

[20] M. Sato and A. J. Sievers, Nature **432**, 486 (2004).

[21] P. G. Kevrekidis, S. V. Dmitriev, S. Takeno, A. R. Bishop, and E. C. Aifantis, Phys. Rev. E **70**, 066627 (2004).

[22] M. Sato, B. E. Hubbard, and A. J. Sievers, Rev. Mod. Phys. **78**, 137 (2006).

[23] V. Hizhnyakov, A. Shelkan, M. Klopov, A. J. Sievers, and M. Haas, Journal of Physics: Conference Series **92** (2007).

[24] M. Kimura and T. Hikihara, Chaos **19**, 13138 (2009).

[25] M. Kimura and T. Hikihara, Physics Letters A **373**, 1257 (2009).

[26] M. Sato and A. Sievers, Journal of Biological Physics **35**, 57 (2009).

[27] B. A. Malomed, P. G. Kevrekidis, D. J. Frantzeskakis, H. E. Nistazakis, and A. N. Yannacopoulos, Phys. Rev. E **65**, 056606 (2002).

[28] L. Q. English, F. Palmero, A. J. Sievers, P. G. Kevrekidis, and D. H. Barnak, Phys. Rev. E **81**, 046605 (2010).

[29] R. B. Thakur, L. Q. English, and A. J. Sievers, Journal of Physics D: Applied Physics **41**, 015503 (2008).

[30] M. Kimura, *Studies on the Manipulation of Intrinsic Localized Modes in Coupled Cantilever Arrays*, Ph.D. thesis, Kyoto University (2008).

[31] D. Cohen-Tanugi, A. Akey, and N. Yao, Nano Letters **10**, 852859 (2010).

[32] S. D. Hersee, X. Y. Sun, X. Wang, M. N. Fairchild, J. Liang, and J. Xu, J. Appl. Phys. **97**, 124308 (2005).

[33] M. Akabori, J. Takeda, J. Motohisa, and T. Fukui, Nanotechnology **14**, 1071 (2003).

[34] J. L. Taraci, J. W. Dailey, T. Clement, D. J. Smith, J. Drucker, and S. T. Picraux, Applied Physics Letters **84**, 5302 (2004).

[35] Q. Li, K. R. Westlake, M. H. Crawford, S. R. Lee, D. D. Koleske, J. J. Figiel, K. C. Cross, S. Fathololoumi, Z. Mi, and G. T. Wang, Opt. Express **19**, 25528 (2011).

[36] D. Gauthier, M. Guizar-Sicairos, X. Ge, W. Boutu, B. Carré, J. R. Fienup, and H. Merdji, Phys. Rev. Lett. **105**, 093901 (2010).

[37] M. Howells and et al, Nuclear Instruments and Methods in Physics Research, Section A **467**, 864 (2001).

[38] H. T. Kim, I. J. Kim, C. M. Kim, T. M. Jeong, T. J. Yu, S. K. Lee, J. H. Sung, J. W. Yoon, H. Yun, S. C. Jeon, I. W. Choi, and J. Lee, Appl. Phys. Lett **98**, 121105 (2011).

[39] D. Sayre, H. N. Chapman, and J. Miao, Acta Crystallographica **54**, 232 (1998).

[40] R. L. Sandberg, A. Paul, D. A. Raymondson, S. Hädrich, D. M. Gaudiosi, J. Holtsnider, R. I. Tobey, O. Cohen, M. M. Murnane, H. C. Kapteyn, C. Song, J. Miao, Y. Liu, and F. Salmassi, Phys. Rev. Lett. **99**, 098103 (2007).

[41] H. N. Chapman and K. A. Nugent, Nature Photonics **4**, 833 (2010).

[42] I. McNulty, J. Kirz, C. Jacobsen, E. H. Anderson, M. R. Howells, and D. P. Kern, Science **256**, 1009 (1992).

[43] B. R. Benware, C. H. Moreno, D. J. Burd, and J. J. Rocca, Optics Lett. **22**, 796 (1997).

[44] C. Macchietto, B. Benware, and J. Rocca, Optics Letters **24**, 1115 (1999).